論文 / 著書情報
Article / Book Information

Title	Comparison of Simulated Plasma Flow Field in a Two-Dimensional MagnetoplasmadynamicThruster With Experimental Data
Author	K.Kubota, I.Funaki, Y.Okuno
Journal/Book name	IEEE Trans. Plasma Science, Vol. 37, No. 12, pp. 2390-2398
Issue date	2009, 12
DOI	http://dx.doi.org/10.1109/TPS.2009.2032913
URL	http://www.ieee.org/index.html
Copyright	(c)2009 IEEE. Personal use of this material is permitted. Permission from IEEE must be obtained for all other users, including reprinting/republishing this material for advertising or promotional purposes, creating new collective works for resale or redistribution to servers or lists, or reuse of any copyrighted components of this work in other works.
Note	このファイルは著者（最終）版です。 This file is author (final) version.

Comparison of Simulated Plasma Flowfield in a Two-dimensional Magnetoplasmadynamic Thruster with Experimental Data

Kenichi Kubota, Ikkoh Funaki, *Member, IEEE*, and Yoshihiro Okuno

***Abstract*—Comprehensive comparisons of the numerically simulated results of the plasma flowfields in a 100 kW class two-dimensional magnetoplasmadynamic thruster with available experimental data are conducted. The propellant is argon of 1.25 g/s and the discharge current is varied from 8 to 12 kA. The physical model includes non-equilibrium single-level of ionization and a collisional-radiative model for argon ion to assess the reaction processes in detail. The data we mainly compared are the current path, the electron number density and the electron temperature. There is qualitative agreement between the calculated and experimental results except for the electron temperature. In order to explain the disagreement of the electron temperature, we estimate the excitation temperature from the distributions of the excited ions in 4s and 4p states, radiation of which was employed to determine the electron temperature in the experiment. As a result, it is found that the calculated excitation temperature becomes close to the measured result, and that the plasma deviates from partial local thermodynamic equilibrium near the anode surface. Regarding the thrust and the thrust efficiency, their features against variation of the discharge current are well captured by the simulation, although they are slightly overestimated compared with measured values.**

***Index Terms*—Electric Propulsion, Magnetoplasmadynamic Thruster, Collisional-Radiative Model**

Nomenclature

$\boldsymbol{B}$ = magnetic flux density
C_s = thermal velocity of species s
c_p = specific heat at constant pressure
$\boldsymbol{E}$ = electric field
e = elementary charge
g_s = statistical weight of species s
F = thrust
$\bar{I}$ = unit tensor
J = total discharge current
$\boldsymbol{j}$ = current density
k = Boltzmann constant
l_s = mean free path of species s
m_s = mass of species s
$\dot{m}$ = mass flow rate
n_s = number density of species s
p = pressure
P_r = Prandtl number
Q_{ij} = collision cross section between particles i and j
q_{rad} = radiative loss
R_m = magnetic Reynolds number
$T_{s,ex}$ = temperature of species s / excitation temperature
$\boldsymbol{u}$ = velocity
U_s = internal energy of species s
$U_{ion,ex}$ = ionization/excitation energy
V = discharge voltage

Manuscript received October 18, 2008. The present research was supported by a Grant-in-Aid from the Japan Society for Promotion of Science.

K. Kubota and I. Funaki is with the Institute of Space and Astronautical Science, Japan Aerospace Exploration Agency, Kanagawa, 229-8510, Japan (e-mail: kubota.kenichi@jaxa.jp, funaki@isas.jaxa.jp).

Y. Okuno are with the Department of Energy Sciences, Tokyo Institute of Technology, Kanagawa, 226-8502, Japan (e-mail: yokuno@es.titech.ac.jp).

$V_{ion,ex}$ = ionization/excitation energy
W = thruster width
x = coordinate
y = coordinate
z = coordinate

η = generalized coordinate / thrust efficiency
λ_s = thermal conductivity of species s
μ = viscosity coefficient
μ_0 = permeability of vacuum
ν_{ij} = collision frequency between particles *i* and *j*
ξ = generalized coordinate
ρ_s = mass density of species s
σ = electrical conductivity
$\overline{\tau}$ = viscous stress tensor
Φ = dissipation function

Subscript

e	electrons
em	electromagnetic
ex	excitation
h	heavy particles (Ar-I, Ar-II)
i	ions
ion	ionization
n	neutrals
s	species
sh	sheath

I. INTRODUCTION

A self-field magnetoplasmadynamic thruster (MPDT) is one of high-power electric propulsion devices for an interplanetary spacecraft [1]. In a discharge chamber of MPDT, the interaction between a discharge current (> 1kA) and an induced magnetic field (~0.1 T) produces Lorentz force to accelerate a plasma initiated by an arc discharge. In general, MPDTs are operated with the electric power from several hundreds of kW to MW, and then relatively high thrust (~10N) can be obtained. Most of the experiments for high power (100 kW ~ MW) MPDT have been conducted with a quasi-steady operation [2], whereas steady-state operations with a power of 200 kW have also been done in Germany [3]. However, in spite of many research activities on MPDTs, thrust efficiency is limited to a low value of less than 30% (with Ar propellant) at the present stage [2]. When hydrogen is used as a propellant, thrust efficiency can be increased above 50% [4], but there remains the problem of a storage system. To further improve the MPDT design for enhancement of thrust efficiency, detailed information on plasma parameters inside the discharge chamber is helpful. However, it is hard to observe the flowfields inside MPD thrusters, because the MPDTs generally consist of coaxial electrodes, i.e. a plasma flow is surrounded by a cylindrical anode, although there have been a variety of plasma diagnoses by means of probe methods [3]-[5].

In order to measure the plasma properties inside an MPDT, a self-field two-dimensional MPDT (2D-MPDT) shown in Fig. 1 was developed by Toki [6]. Using the 2D-MPDT, an optical access to the two-dimensional flow became possible. Also, measurements of the magnetic field distribution corresponding to current contours could also be performed [6]-[9]. Actually, the 2D-MPDT was contrived mainly for the purpose of observations of plasma flows, but two-dimensional imaging data of plasma in a 2D-MPDT are very fruitful not only to comprehend accelerating thermochemical non-equilibrium flows within MPDTs but also to construct a physical model, although it may be difficult for 2D-MPDTs to precisely reproduce the features of coaxial MPDTs. It is also possible to validate a numerical code by comparing the measured imaging data of 2D-MPDT with the calculated results. Through the discussion on the relationship between the thrust characteristics and the flowfield parameters, the validated code will contribute to find a design policy of an MPDT with preferred acceleration mechanisms.

Although thrust performance data as well as plasma flow data for a variety of experimental conditions are available, intensive numerical investigations for 2D-MPDTs with a detailed physical model have not been performed, whereas a number of investigations on coaxial MPDTs have been conducted [10]-[13]. There exist some comparisons of the simulated flowfieds of coaxial thrusters to the experimental results [10]-[12], but the counterpart for 2D-MPDTs is limited to the work of [9] in which a fairly simple model was used. Recently, the effects of thruster geometry on flowfields and performance of 2D-MPDT were examined by the authors [14]. The present effort focuses on comparison of the available experimental data with the numerical results obtained from our advanced code which was originally developed in the work of [9]. The flowfield of a 100-kW-class 2D-MPDT with Ar propellant is simulated by the code in which non-equilibrium single-level of ionization, thermal non-equilibrium, viscosity, thermal conduction, and the Hall effect, all of which were ignored in [9], are incorporated. Additionally, the present model includes collisional-radiative (CR) processes of Ar-II, which has not been taken into account in the other numerical studies. Since the measured electron temperature was evaluated with the relative intensity of Ar-II lines, inclusion of the CR model for Ar-II is expected to provide some insights in the discussion on the electron temperature. With this model, we can examine the validity of assumption of partial local thermodynamic equilibrium in the flowfield. Moreover, direct comparison of the distribution of the excited ions with the radiative intensity observed in the experiment is possible. The performances such as the thrust and the thrust efficiency are also discussed.

II. NUMERICAL MODELING

A. *Thruster Geometries and Computational Region*

The thruster adopted here consists of a flared anode and a short cathode with a conical tip as shown in Fig. 2. In accordance with the geometry used in the experiments [6]-[9], the inner interval between the anodes is set to 28 mm at the inlet, and 56 mm at the outlet of the thruster. The cathode has a thickness of 8 mm. The width of the thruster W is assumed as a constant of 80 mm. The computational region is limited to upper half domain, and is extended toward the downstream domain up to 100 mm in the streamwise direction.

B. *Physical Modeling*

Argon is used as a propellant, and single-level of ionization is taken into account as a non-equilibrium process. In addition, collisional-radiative processes of Ar-II are incorporated. We assumed the flow is completely uniform in the z direction in the formulation. The Navier-Stokes equation with the MHD effects, and the induction equation, which determines the induced magnetic field, have to be solved. The governing equations are as follows.

Total mass

$$\frac{\partial \rho}{\partial t} + \nabla \cdot (\rho \boldsymbol{u}) = 0 . \tag{1}$$

Mass of ions

$$\frac{\partial \rho_s}{\partial t} + \nabla \cdot (\rho_s \boldsymbol{u}) = \dot{\rho}_s . \tag{2}$$

Momentum

$$\frac{\partial \rho \boldsymbol{u}}{\partial t} + \nabla \cdot \left[\rho \boldsymbol{u}\boldsymbol{u} + \left(p + \frac{\boldsymbol{B}^2}{2\mu_0} \right) \bar{I} - \frac{\boldsymbol{B}\boldsymbol{B}}{\mu_0} \right] = \nabla \cdot \bar{\tau} . \tag{3}$$

Internal energy of heavy particles

$$\frac{\partial U_h}{\partial t} + \nabla \cdot (U_h \boldsymbol{u}) = -p_h \nabla \cdot \boldsymbol{u} + \Phi + \nabla \cdot (\lambda_h \nabla T_h) + \delta E . \tag{4}$$

Internal energy of electrons, ionization energy, and excitation energy

$$\frac{\partial}{\partial t}(U_e + U_i + U_{ex}) + \nabla \cdot [(U_e + U_i + U_{ex})\boldsymbol{u}] = -p_e \nabla \cdot \boldsymbol{u} + \frac{\boldsymbol{j}^2}{\sigma} + \nabla \cdot (\lambda_e \nabla T_e) + \frac{5k}{2e} \boldsymbol{j} \cdot \nabla T_e - \delta E - q_{rad} . \tag{5}$$

Induction equation

$$\frac{\partial \boldsymbol{B}}{\partial t} - \nabla \times (\boldsymbol{u} \times \boldsymbol{B}) = -\nabla \times \left[\frac{1}{\mu_0 \sigma} \nabla \times \boldsymbol{B} + \frac{1}{\mu_0 e n_e} (\nabla \times \boldsymbol{B}) \times \boldsymbol{B} \right] . \tag{6}$$

The right hand side of (2) denotes the reaction source terms. The excitation of Ar-I and the ionization from Ar-II to Ar-III are not taken into account since it was reported that the intensity of the spectral lines of Ar-I and Ar-III were far less than that of Ar-II in the 2D-MPDT [3], whereas it was shown that Ar plasma in a coaxial MPDT generally contains Ar-III and even Ar-IV [15]. For the ionization process, Lotz formula is utilized as the forward reaction rates [16], and three-body recombination rate is calculated with detailed balancing relationship. The collisional-radiative (CR) model for Ar-II employed in this study deals with the interactions among the doublet ions, where some degenerate levels are modeled as a homogeneous group [17]. In this study, the uppermost energy level is limited to 4p orbit for simplicity, thus the states for Ar-II of 3p (ground), 4s, 3d, and 4p are involved in accordance with the model, where the 3d level is divided into three groups (^{2}P, ^{2}F$_{5/2}$), ^{2}F$_{7/2}$, and ^{2}D. Regarding the excitation rate, we utilized the formula given by Rubin and Sobolev [18] for all reactions except for 3p-3d (^{2}P, ^{2}F$_{5/2}$), 3p-3d (^{2}D), 3d (^{2}P, ^{2}F$_{5/2}$)-4p, and 3d (^{2}D)-4p for which Beigman's data are utilized [19]. As for the radiative process, we assumed that the plasma is optically thick towards the ground state, and is optically thin for the inter-level transfers [20]. The internal energy of the heavy particles and electrons are defined as

$$U_h = \frac{3}{2} n_h k T_h, \qquad U_e = \frac{3}{2} n_e k T_e . \tag{7}$$

The ionization energy U_i and excitation energy U_{ex} are given by

$$U_i = V_i \sum_{ion} n_s, \qquad U_{ex} = \sum_{ex} V_{ex} n_s , \tag{8}$$

where the summation is taken for the ions and the excited ions respectively. The δE in the Eq. (4), (5) denotes the energy exchange rate between the heavy particles and electrons [21]. The q_{rad} in Eq. (5) corresponds to the radiation loss relating the inter-level transfers of Ar-II. The current density is obtained from Ampère's law, and the equation of state is necessary for closed formulation.

$$\boldsymbol{j} = \frac{1}{\mu_0} \nabla \times \boldsymbol{B} , \tag{8}$$

$$p = n_h k T_h + n_e k T_e . \tag{9}$$

In this study, the ideal equation of state is assumed to be valid. The governing equations (1)-(6) are solved numerically by a time marching method. The convective terms are evaluated with the second order Lax-Friedrich TVD scheme [22],[23]. The electrical conductivity is determined by [24]

$$\sigma = \frac{e^2 n_e}{m_e \nu_{eh}} , \tag{11}$$

and the viscous coefficient adaptable for partially ionized gas is given by [25]

$$\mu = \frac{1}{2} \alpha m_h C_h \sum_{s \neq e} n_s l_s , \tag{12}$$

where α is a constant slightly less than unity. The thermal conductivities of the heavy particles and the electrons are calculated from the relations below [24], where the Prandtl number P_r is assumed to be 2/3 in this study;

$$\lambda_h = \frac{\mu c_p}{P_r}, \qquad \lambda_e = \frac{2.4}{1 + \nu_{ei} / \nu_{eh} \sqrt{2}} \frac{k^2 n_e T_e}{m_e \nu_{eh}} . \tag{13}$$

Here, the collision cross sections are required to evaluate the collision frequencies. We use $Q_{in} = 8 \times 10^{-19}$ m^2 [26], and the following relations [24],[27],[28];

$$Q_{si} = \frac{5.85 \times 10^{-10}}{T_s^{\ 2}} \ln \left[1.24 \times 10^7 \left(\frac{T_e^{\ 3}}{n_e} \right)^{1/2} \right] , \tag{14}$$

$$Q_{en} = \frac{2.336 \times 10^{-14}}{C_e} \left(\frac{kT_e}{e} \right)^{1.609} \exp \left[0.0618 \left(\ln \frac{kT_e}{e} \right)^2 - 0.1171 \left(\ln \frac{kT_e}{e} \right)^3 \right] , \tag{15}$$

$$Q_{nn} = 2.57 \times 10^{-19} \left(1 + \frac{169.9}{T_h} \right) . \tag{16}$$

C. Boundary Conditions

The prescribed mass flow rate of 1.25 g/s is set at the inlet. Since the plasma ignition process at the inlet is too complex to take into account in the numerical simulation, we ignore the processes and assume that a relatively high temperature and highly ionized plasma inflows into the thruster. In this calculation, the plasma at the inlet is assumed to have the heavy particle temperature of 5,000 K and the electron temperature of 10,000 K. The degree of ionization at the inlet is set to 0.1. When the flow is subsonic at the inlet, the pressure is extrapolated. On the electrodes, the heavy particle temperature is set to 1,300 K on the anode surface and to 2,000 K on the cathode surface, which are set below the melting points of cupper and Th-loaded tungsten used in the experiments for the anode and the cathode respectively. For the electron temperature along the wall, the adiabatic condition is assumed. As for the boundary conditions for the outflow, zero-order extrapolation is used for the flow variables for simplicity. Although there is a subsonic outflow near the insulator, any harmful influence on the results does not appear. The calculation condition is summarized in Table I. It was confirmed that the calculated results are insensitive to these input parameters.

The total discharge current J is varied over the range of 8 - 12 kA. From the discharge current, the magnetic flux density at the inlet can be determined based on the Ampère's law;

$$B_{in} = -\frac{\mu_0 J}{2W} . \tag{17}$$

This inlet condition for the induced magnetic field assumes that the cathode is forced to emit the electrons supplying a given discharge current J. The actual attainable current density on the cathode will depend on cathode temperature and cathode's material, but the employed cathode size is considered to be enough to supply the given discharge current because of the experimental evidence. Along the electrodes, it is assumed that the surfaces are equipotential, and there exists a uniform sheath. The magnetic flux density on the electrodes is determined from the equipotential condition that the electric field parallel to the electrodes is set to zero. This reduces to the following expression (for dimensionless magnetic field $\hat{B}_z$) by means of generalized Ohm's law;

$$\frac{\partial \hat{B}_z}{\partial \eta}\left[\frac{1}{R_m}\left(\xi_x\eta_y - \xi_y\eta_x\right) + \frac{\beta_e}{R_m}\left(\xi_x\eta_x + \xi_y\eta_y\right)\right] + \frac{\partial \hat{B}_z}{\partial \xi}\frac{\beta_e}{R_m}\left(\xi_x^2 + \xi_y^2\right) = 0 . \tag{18}$$

Here, ξ and η are generalized coordinates corresponding to the tangential and normal directions respectively. Note that $B_z < 0$ is assumed in Eq. (18). The β_e denotes the Hall parameter defined by,

$$\beta_e = \frac{|B_z|\sigma}{e n_e} . \tag{19}$$

The magnetic flux density is set to zero on the insulator, because the sum of the incoming and outgoing current through the outlet of the thruster (z = 45 mm) is zero. At the boundary of the outflow, zero-order extrapolation is used for the magnetic field for simplicity.

III. NUMERICAL RESULTS AND DISCUSSION

A. Comparison of flowfield

Comparisons with the experimental data of 2D-MPDT enable us to validate the numerical result. As for the flowfield data within the thruster, the current path, electron number density, and electron temperature are available so far. In the experiments conducted by Toki [6], Nakayama [7], and Funaki [8], [9], the current path was measured with a magnetic-sensitive film inserted into the discharge camber which reveals the magnetic field strength from darkness patterns. The electron number density was measured by the Mach-Zehnder interferometry [7], [8] or the absolute intensity method [6]. Regarding the electron temperature distribution, a relative intensity method of spectroscopy was employed [7].

Current path

The numerical and the experimental results of the current path for J = 12 kA are shown in Fig. 3. The labeled values on the contour lines denote the ratio of the current flowing upstream viewed from the line to the total discharge current. The calculated result shows that, in the flared region, the current path is obliquely skewed due to the Hall effect [13], where the highest Hall parameter amounts to about 40 in the vicinity of the anode surface. The increase in the Hall parameter is attributed to depletion of the plasma density due to expansion in the flared nozzle as will be shown later. Although this obliquely skewed current path, especially near the anode surface, seems not to appear obviously in the experimental results, it will be appropriate to suppose that both the numerical and experimental results suggest about 20-30% of the discharge current concentrates at the anode edge. Without incorporating the Hall effect, the current concentration at the anode edge cannot be obtained as indicated in [9].

There are still discrepancies between the calculated current paths and the measured data. In the calculated results, the current path near the anode surface is almost parallel to the anode, but the tendency cannot be found in the measured data specifically. The difference may be attributed to the existence of nonuniform sheath on the anode, which is ignored in the simulation. In addition, since the Hall parameter near the anode of the present result is quite high, the plasma may deviate from the fluid approximation. However, the Hall parameter may be decreased when the effect of anomalous resistivity is taken into account in the electrical conductivity model, because the effect of anomalous transportation increases effective collision frequency of the charged particles [29]. Then, the distortion of current may be suppressed due to a decrease in the effective Hall parameter.

From a standpoint of the experiments, we have to take into account the accuracy of the measurement with a magnetic film. It has to be noted that the two experimental results in Fig. 3 do not exactly accord with each other, which indicates that there may be non-negligible uncertainty even in the experiments. Considering that the experimental data were obtained with a single shot, and the sensitivity of a magnetic film for a weak magnetic field is low, the measured current paths around the downstream region, hence near the flared anode surface, can involve an error about 10% or more. In addition, in the vicinity of the electrodes, there may be considerable errors due to a three-dimensional effect caused by the segmented electrode design shown in Fig. 1.

Electron number density

The numerical and the experimental results of the electron number density n_e for J = 12 kA are shown in Fig. 4. The numerical result shows n_e amounts to the maximum about 2.6×10^{21} m^{-3} around the cathode. The calculated value lies between the experimental results of Figs. 4-(b) and 4-(c), although there is considerable quantitative difference between the two experimental results. The increased density at the cathode tip, which can also be seen in Fig. 4-(b), is attributed to the pinch force enhanced by the Hall effect leading to the obliquely skewed current profile. The obvious density increment at the cathode tip did not appear in the work of [9] ignoring the Hall effect. In the vicinity of the flared anode surface, n_e is considerably lower than that in the other region due to the pinch force and expansion through the flared nozzle. This property cannot be seen from the experimental results due to their low resolution in that region, because the fringe shifts of Mach-Zehder interferometry, from which n_e was estimated, becomes unclear with decreasing n_e. In the numerical result, there exists the region with high electron number density around the cathode-side due to intensive current concentration. This tendency can also be seen from the experimental data. It can be seen that the simulated result predicts an existence of a compression wave extended from the cathode tip where the plasma is compressed by pinch force. However, the compression wave cannot be recognized in the experimental data specifically. Since a hemispherical cathode tip employed in the experiment is modeled by the conical cathode tip for simplicity, the simulated compression wave may be accentuated.

Electron temperature

In the previous numerical study [9], fully ionized and thermal equilibrium (T_h = T_e) plasma flow was assumed, and then quantitative comparison between the numerical and experimental results was not conducted. Here we discuss the electron temperature distribution more closely. In Fig. 5, the numerical and the experimental results of the electron temperature T_e are shown. According to the experimental result, T_e amounts to about 2.5 eV at the cathode tip and around the inlet part, while it is no more than 1.2 eV near the anode surface. On the other hand, T_e of the numerical result ranges from about 3.2 eV around the cathode tip to about 4 eV near the anode surface. This qualitative tendency can also be seen even if the electron temperature is limited to a particular value on the anode in order to take into account energy loss of electrons on the anode. The reason for the high electron temperature near the anode is attributed to the depletion of the plasma density as shown in Fig. 4-(a). While the measured T_e in the experiment near the anode is less than that near the cathode, the calculated T_e near the anode is higher than that near the cathode. This discrepancy will need careful discussion.

Different from a coaxial MPDT, in 2D-MPDT, the current density near the anode is not much lower than that near the cathode because of its configuration. Thus if the plasma density near the anode is lower than that near the cathode, the Joule heating per unit mass near the anode can become higher than that near the cathode, which may result in higher electron temperature near the anode. From this standpoint, the calculated result seems reasonable. The current density near the cathode, however, is higher than that near the anode due to the small cathode size compared with the anode, thus the Joule heating per unit volume around the cathode will be higher than that near the anode. Therefore the tendency observed in the experiment also seems acceptable.

In order to explain this discrepancy, we pay attention to the method of the electron temperature measurement. The two-dimensional image of T_e given in [7] was obtained with a relative intensity method, where the intensity of spectral lines of Ar-II was utilized, and then the electron temperature was estimated with the assumption of partial local thermodynamic equilibrium (LTE). Therefore, if we can compute the distribution of the excited ions of Ar-II associated with the utilized spectral lines without partial LTE assumption, we can estimate the excitation temperature T_{ex} by assuming partial LTE relation for the obtained populations of the excited ions. This calculated T_{ex} is considered to correspond to the measured T_e. According to the wavelength found in [7], the radiated light with regard to the transition from 4p to 4s orbit was mainly used for the measurement. Thus the excitation temperature T_{ex} can be defined as follows.

$$\frac{n_{4\mathrm{p}}}{n_{4\mathrm{s}}} = \frac{g_{4\mathrm{p}}}{g_{4\mathrm{s}}} \exp\left[-\frac{e\left(V_{4\mathrm{p}} - V_{4\mathrm{s}}\right)}{kT_{ex}} \right] \tag{20}$$

The distribution of the excitation temperature calculated with the number densities of ions in 4s and 4p levels is shown in Fig. 6. The excitation temperature has a maximum about 3 eV around the cathode, and has relatively lower value of 1-2 eV near the anode. This qualitative tendency agrees well with the measured electron temperature. Strictly speaking, there is still qualitative disagreement resulting from the appearance of the compression wave in the calculation as shown above. In addition, because of the simplicity of the employed CR model and the fact that the accuracy of the excitation cross sections used here is at best a factor 2 [17], quantitative discussion will be inappropriate. Nonetheless, the calculated T_{ex} has the relatively similar value to the measured data, which may be due to the fact that the excitation temperature depends only on the ratio of the number densities, i.e. involved errors may be canceled. Comparing the calculated T_e with T_{ex}, these are comparable around the cathode, therefore it can be said that the assumption of partial LTE seems valid around the cathode. On the other hand, near the flared anode surface, T_{ex} is less than T_e, thus the plasma is supposed to deviate from partial LTE because of the low plasma density. These results suggest that the measured electron temperature is underestimated near the anode surface, in other words, there is a possibility that the actual electron temperature is much higher than the measured values near the anode surface.

Distribution of excited ions

The calculated distribution of number density of the excited ion in 4p level can be compared with the radiative intensity map representing relative spectral intensity proportional to the population density [6]. Strictly speaking, comparison between the numerical and the experimental result may not be appropriate, because the observed radiation (480.6 nm) is attributed to the transition between quartet states of 4p - 4s levels, and in our model, the interaction only among the doublet states are dealt with. Even then it will be useful to show the distribution of the irradiating excited ions in 4p level. As shown in Fig. 7, the calculated result shows that the 4p ions are distributed mainly around the cathode, which seems similar to the observed intensity map. On the contrary, there are few 4p ions near the anode regardless of high electron temperature, which is due to the rarefaction of the plasma. On the whole, the number densities of the excited ions are much less than those of the ions in ground state, thus whether the CR model is incorporated in the model does not affect the overall flowfields and the performance significantly.

B. *Performance Evaluation*

The purpose of this section is to compare the performance such as thrust, and thrust efficiency with the experimental results.

Thrust

The thrust F is computed from a momentum flux at the thruster exit.

$$F = \int_{exit} \left(\rho u^2 + p\right) dS \tag{21}$$

Generally, the thrust evaluated via above equation includes both an electrothermal thrust and an electromagnetic thrust. A reaction force of the electrothermal thrust acts on the electrodes though the pressure, and a reaction force of the electromagnetic force acts on an electric circuit of the discharge. The component of the electromagnetic thrust F_{em} can be computed by a volume integral of the Lorentz force in x direction.

$$F_{em} = \int_V \left(\boldsymbol{j} \times \boldsymbol{B}\right)_x dV \tag{22}$$

Given an ideal condition such as a straight anode, a theoretical electromagnetic thrust can be derived as the following equation in which the effect of the Lorenz force in x direction and the pressure force acting on the cathode surface are included [30].

$$F_{em} = \frac{\mu_0 d_a}{8W} J^2 \tag{23}$$

Here, d_a denotes an interval between the upper and lower anodes. In Fig. 8, the total thrust F, the measured thrust [31], and the electromagnetic thrust F_{em} are plotted, and the theoretical curve of F_{em} is also described. As the value of d_a in Eq. (23), the anode interval at the inlet is substituted, because most of the discharge current concentrates around the upstream region. It can be seen that the calculation overestimates the total thrust about 1 N. The reason for this will be attributed to the fact that both side of the MPD thruster was normally covered by quartz glass during the thrust measurement, which will cause the thrust reduction via friction loss. In addition, the actual experimental apparatus will have the end effect at the both side of the thruster, which means deviation from the complete two-dimensional uniformity of the induced magnetic field in z direction. Since the actual induced magnetic field at the side is less than that at the center of the thruster, the electromagnetic thrust will be reduced compared with the ideal condition. Regarding the electromagnetic thrust, the calculated value is in good agreement with the theoretical curve. Also, the result indicates that the electromagnetic thrust amounts to 65% of the total thrust at $J = 12$ kA, while it is 43% at $J = 8$ kA. Hence it can be said, in terms of the ratio of F_{em} to F, the acceleration mode is changed from the electrothermal to the electromagnetic between $J = 8$ and 12 kA.

Thrust efficiency

A thrust efficiency is defined as the ratio of a kinetic energy of the plasma at the thruster exit to an input power. With the thrust F, the thrust efficiency η can be given by the following equation,

$$\eta = \frac{F^2}{2\dot{m}J\left(V + V_{sh}\right)} \tag{24}$$

where V and V_{sh} denotes a voltage drop in the bulk plasma and a sheath voltage respectively. The voltage drop in the bulk plasma is given by a line integral of the electric field from the anode to the cathode. For $J = 8$, 10, 12 kA, V is 8.0, 10.1, and 12.6 V respectively. Since the sheath effect is not included in the present model, we assume V_{sh} to obtain the thrust efficiency. Although there are not comprehensive understandings on the sheath voltage drop in an MPD thruster, the sum of an anode sheath drop and a cathode sheath drop is supposed to range from 20 to 40 V [32].

In Fig. 9, the thrust efficiencies of the numerical and the experimental results are plotted. Regarding the numerical results, the closed square plots are given under the condition of V_{sh} = 30 V, and the top and the bottom of the error bar corresponds to the thrust efficiency for V_{sh} = 20 and 40 V respectively. It can be seen that, although qualitative feature of the thrust efficiency is well captured, the numerical results overestimate the experimental values probably due to the difference in the thrust F as mentioned above. In addition, the uncertainty of the sheath voltage makes it difficult to predict the thrust efficiency. Judging from the calculated voltage drop in the bulk plasma V and the discharge voltage obtained from the experiment, the total sheath voltage drop is inferred to be about 40 V. However, there is a possibility for the calculation to underestimate the voltage drop in the bulk plasma, since the effect of anomalous resistivity which will decrease the conductivity of the plasma is not included in the present model [29].

IV. CONCLUSION

We have developed the numerical code with the detailed modeling to simulate flowfields of a self-field two-dimensional magnetoplasmadynamic thruster, and have compared the simulated plasma flow and the performance with the experimental results. In the physical model, non-equilibrium ionization of argon propellant and the collisional-radiative model of Ar-II are incorporated in order to examine the detailed reaction processes.

The results show that the current path is obliquely skewed in the thruster due to the Hall effect, which can be seen in the measured data, although the distortion of the calculated current path in the vicinity of the flared anode surface appears excessively. The distribution of the electron number density around the cathode is well captured by the calculation, although quantitative argument remains. The distribution of the electron temperature, however, differs qualitatively from the measured result obtained with a relative intensity method. Since the measured result should be interpreted not as translational electron temperature but as excitation temperature, we numerically estimate the excitation temperature from the calculated populations of the excited ions in 4s and 4p levels. Consequently, it is shown that the calculated excitation temperature becomes close to the measured result, and is suggested that the plasma deviates from partial local thermodynamic equilibrium (LTE) near the flared anode surface, while the partial LTE assumption seems valid around the cathode.

The computed characteristics of the thrust and the thrust efficiency against variation of the discharge current are almost the same with the experimental result, although the calculated values are slightly overestimated.

The effects of the anomalous resistivity on the electron temperature may have to be examined, since it may affect on the current distortion near the anode surface.

ACKNOWLEDGMENT

We would like to express an acknowledgement to the Engineering and Digital Innovation Center at Japan Aerospace Exploration Agency, and Global Scientific Information and Computing Center at Tokyo Institute of Technology.

REFERENCES

[1] M. Martinez-Sanchez, and J. E. Polland, “Spacecraft Electric Propulsion – An Overview,” *J. Propul. Power*, Vol. 14, No. 5, 1998, pp. 688-699.

[2] E. Y. Choueiri, and J. K. Ziemer, “Quasi-Steady Magnetoplasmadynamic Thruster Performance Database,” *J. Propul. Power*, Vol. 17, No. 5, 2001, pp. 967-976.

[3] H. L. Kurtz, M. Auweter-Kurtz, W. Merke, and H. O. Schrade, “Experimental MPD Thruster Investigations,” AIAA Paper 87-1019, 1987.

[4] H. Tahara, Y. Kagaya, and T. Yoshikawa, “Hybrid MPD Thruster with Axial and Cusp Magnetic Fields,” 20th International Electric Propulsion Conf., IEPC Paper 88-058, 1988.

[5] A. D. Gallimore, A. J. Kelly, and R. G. Jahn, “Anode Power Deposition in Magnetoplasmadynamic Thrusters,” *J. Propul. Power*, Vol. 9, No. 3, 1993, pp. 361-368.

[6] K. Toki, M. Sumida, and K. Kuriki, “Multichannel Two-Dimensional Magnetoplasmadynamic Ardjet,” *J. Propul. Power*, Vol. 8, No. 1, 1992, pp. 93-97.

[7] T. Nakayama, K. Toki, and K. Kuriki, “Quantitative Imaging of the Magnetoplasmadynamic Flowfield,” *J. Propul. Power*, Vol. 8, No. 6, 1992, pp. 1217-1223.

[8] I. Funaki, K. Toki, and K. Kuriki, “Electrode Configuration Effect on the Performance of a Two-Dimensional Magnetoplasmadynamic Arcjet,” *J. Propul. Power*, Vol. 14, No. 6, 1998, pp. 1043-1048.

[9] I. Funaki, K. Toki, and K. Kuriki, “Numerical Analysis of a Two-Dimensional Magnetoplasmadynamic Arcjet,” *J. Propul. Power*, Vol. 13, No. 6, 1997, pp. 789-795.

[10] P. G. Mikellides, “Modeling and Analysis of a Megawatt-Class Magnetoplasmadynamic Thruster,” *J. Propul. Power*,Vol. 20, No. 2, 2004, pp.204-210.

[11] J. Heiermann, and M. Auweter-Kurtz, “Numerical and Experimental Investigation of the Current Distribution in Self-Field Magnetoplasmadynamic Thrusters,” *J. Propul. Power*, Vol. 21, No. 1, 2005, pp. 119-128.

[12] K. Sankaran, E. Y. Choueiri, and S. C. Jardin, “Comparison of Simulated Magnetoplasmadynamic Thruster Flowfields to Experimental Measurements,” *J. Propul. Power*, Vol. 21, No. 1, 2005, pp.129-138.

[13] K. Kubota, I. Funaki, and Y. Okuno, “Numerical Study of Plasma Behavior in a Magnetoplasmadynamic Thruster Around Critical Current,” *J. Propul. Power*, Vol. 25, No. 2, 2009, pp. 397-405.

[14] K. Kubota, I. Funaki, and Y. Okuno, “Numerical Study of Electrode Geometry Effects on Flowfield in Two-dimensional MPD thrusters,” 30th International Electric Propulsion Conf., IEPC Paper 2007-87, 2007.

[15] A. P. Bruckner, and R. G. Jahn, “Exhaust Plume Structure in a Quasi-Steady MPD Accelerator,” *AIAA Journal*, Vol. 12, No. 9, 1974, pp. 1198-1203.

[16] W. Lotz, “Electron-Impact Ionization Cross-Sections and Ionization Rate Coefficients for Atoms and Ions from Hydrogen to Calcium,” *Zeitschrift für Physik*, Vol. 216, 1968, pp. 241-247.

[17] B. F. M. Pots, B. Van Der Sijde, and D. C. Schram, “A Collisional Radiative Model for the Argon Ion (Laser) System with an Experimental Test,” *Physica*, 94C, 1978, pp. 369-393.

[18] P. L. Rubin, and N. N. Sobolev, “Elementary Processes and the Mechanism of Populating the Working Levels in a Continuous-wave Ion Argon Laser,” *Sov. Phys. JETP.*, Vol. 41, No. 5, 1976, pp. 848-854.

[19] I. L. Beigman, L. A. Vainshtein, P. L. Rubin, and N. N. Sobolev, “Mechanism of Generation Excitation in a Continuously Operating Argon Ion Laser,” *JETP Lett.*, 6, 1968, pp. 343-345.

[20] E. J. Sheppard, and M. Martinez-Sanchez, “Nonequilibrium Ionization in Plasma Accelerators,” AIAA paper 90-2608, 1990.

[21] G. W. Sutton, and A. Sherman, *Engineering Magnetohydrodynamics*, New York: Dover, 2006.

[22] G. Tóth, and D. Odstrčil, “Comparison of Some Flux Corrected Transport and Total Variation Diminishing Numerical Schemes for Hydrodynamic and Magnetohydrodynamic Problems,” *J. Comput. Phys.*, Vol. 128, 1996, pp. 82-100.

[23] H. C. Yee, “A Class of High-Resolution Explicit and Implicit Shock-Capturing Methods,” NASA TM-101088, 1989.

[24] M. Mitchner, and C. H. Kruger, *Partially Ionized Gases*, John Wiley & Sons, 1973.

[25] P. G. Mikellides, P. J. Turchi, and N. F. Roderick, “Applied-Field Magnetoplasmadynamic Thruters, Part 1: Numerical Simulations Using the MACH2 Code,” *J. Propul. Power*, Vol. 16, No. 5, 2000, pp.887-893.

[26] C. Boie, M. Auweter-Kurtz, H. J. Kaeppeler, and P. C. Sleziona, “Numerical Investigation of MPD Thrusters with Unstructured Mesh Methods,” 24th International Electric Propulsion Conf., IEPC Paper 95-168, 1995.

[27] M. A. Lieberman, and A. J. Lichtenberg, *Principles of Plasma Discharges and Materials Processing*, 2nd ed., John Wiley & Sons, 2005.

[28] K. Fujita, “Arc Column Behavior and Heat Loss Mechanism in a DC Arcjet Thruster,” Ph.D. Dissertation, Univ. of Tokyo, 1994.

[29] E. Y. Choueiri, “Anomalous resistivity and Heating in Current-driven Plasma Thrusters,” *Phys. Plasmas*, Vol. 6, No. 5, 1999, pp. 2290-2306.

[30] T. Nakayama, “Plasma Acceleration Process in the MPD Arcjet,” Ph. D. Dissertation, Univ. of Tokyo, 1991.

[31] I. Funaki, “Magnetohydrodynamic Flow in MPD Arcjet,” Ph. D. Dissertation, Univ. of Tokyo, 1995 (in Japanese).

[32] K. Kuriki, M. Onishi, and S. Morimoto, “Thrust Measurement of KIII MPD Arcjet,” *AIAA Journal*, Vol. 20, No. 10, 1982, pp. 1414-1419.

TABLE I
Calculation Conditions

Propellant	Ar
Mass flow rate (g/s)	1.25
Discharge current (kA)	8 - 12
T_h at inlet (K)	5,000
T_e at inlet (K)	10,000
Degree of Ionization at inlet	0.1
T_h on anode (K)	2,000
T_h on cathode (K)	1,300
T_e on electrodes	Adiabatic

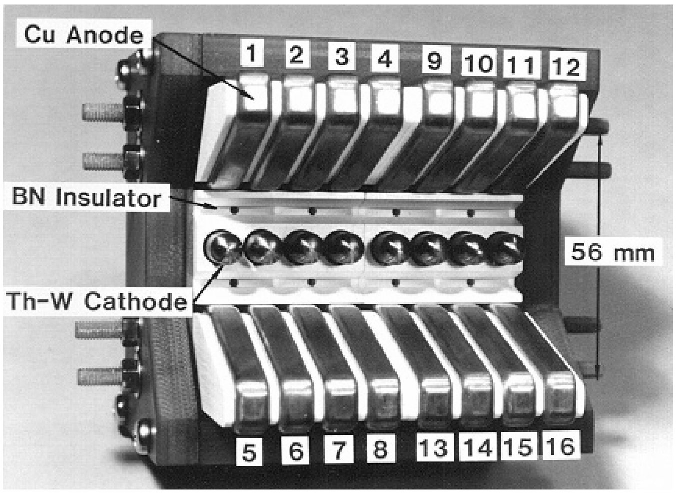

Fig. 1. Self-field two-dimensional MPD thruster (From K. Toki, M. Sumida, and K. Kuriki [6], reprinted with permission of the American Institute of Aeronautics and Astronautics, Inc.).

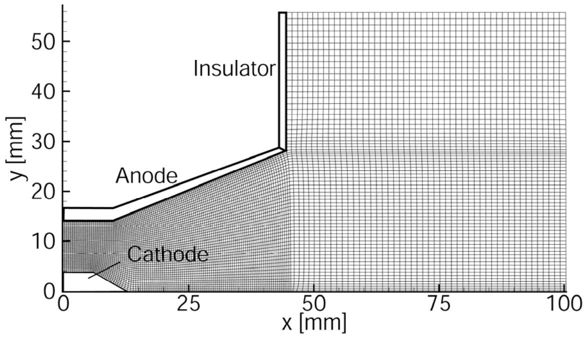

Fig. 2. Thruster geometry and computational region.

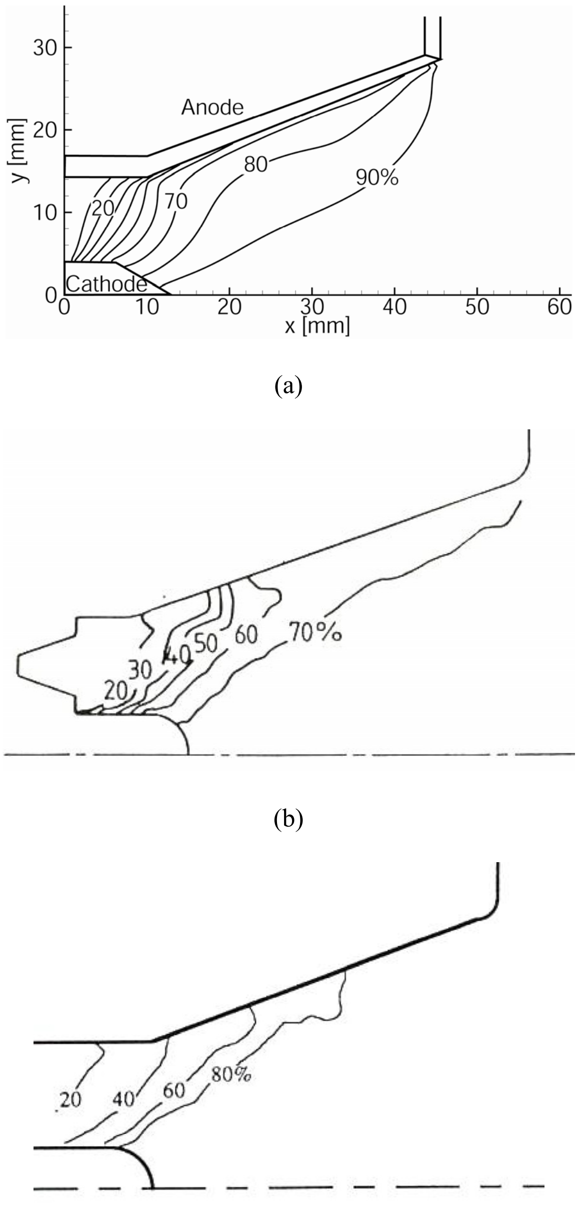

(a)

(b)

(c)

Fig. 3. Current path, Ar, 1.25 g/s, $J = 12$ kA, (a) Calc., (b) Exp. (From K. Toki, M. Sumida, and K. Kuriki [6]) , (c) Exp. (From I. Funaki, K. Toki, and K. Kuriki [9]), (b) and (c) are reprinted with permission of the American Institute of Aeronautics and Astronautics, Inc..

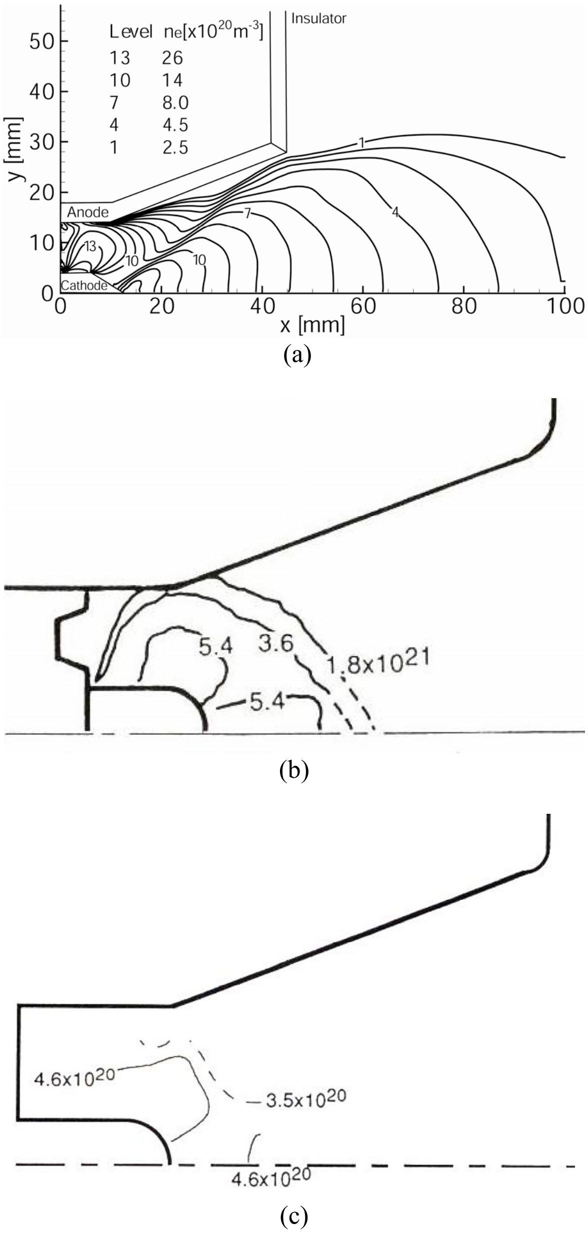

(a)

(b)

(c)

Fig. 4. Electron number density, m^{-3}, Ar, 1.25 g/s, $J = 12$ kA, (a) Calc., (b) Exp. (From T. Nakayama, K. Toki, and K. Kuriki [7]), (c) Exp. (I. Funaki, K. Toki, and K. Kuriki [8]), (b) and (c) are reprinted with permission of the American Institute of Aeronautics and Astronautics, Inc..

.

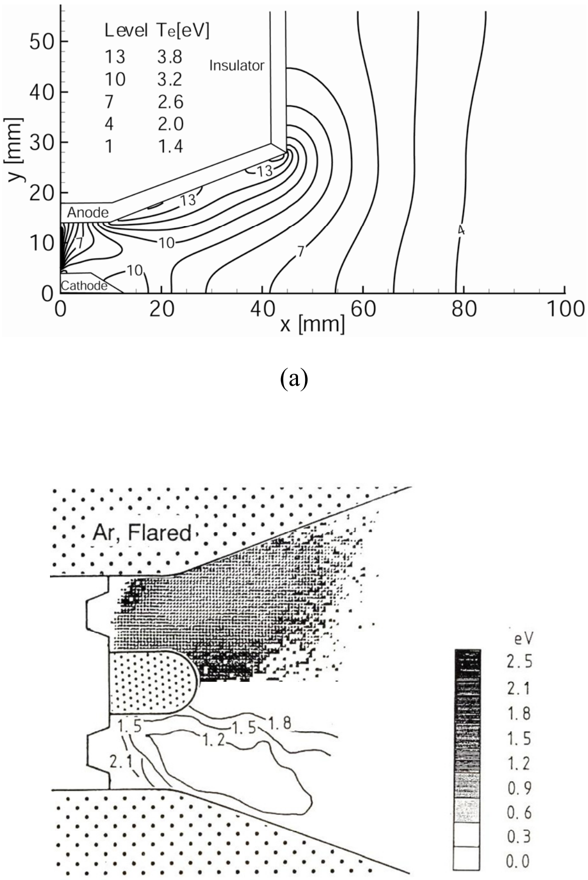

(a)

(b)

Fig. 5. Electron temperature, eV, Ar, 1.25 g/s, $J = 12$ kA, (a) Calc., (b) Exp. (From T. Nakayama, K. Toki, and K. Kuriki [7], reprinted with permission of the American Institute of Aeronautics and Astronautics, Inc.)[7].

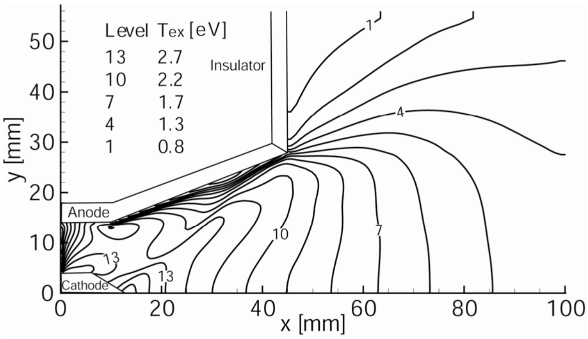

Fig. 6. Excitation temperature, eV, Ar, 1.25 g/s, $J = 12$ kA.

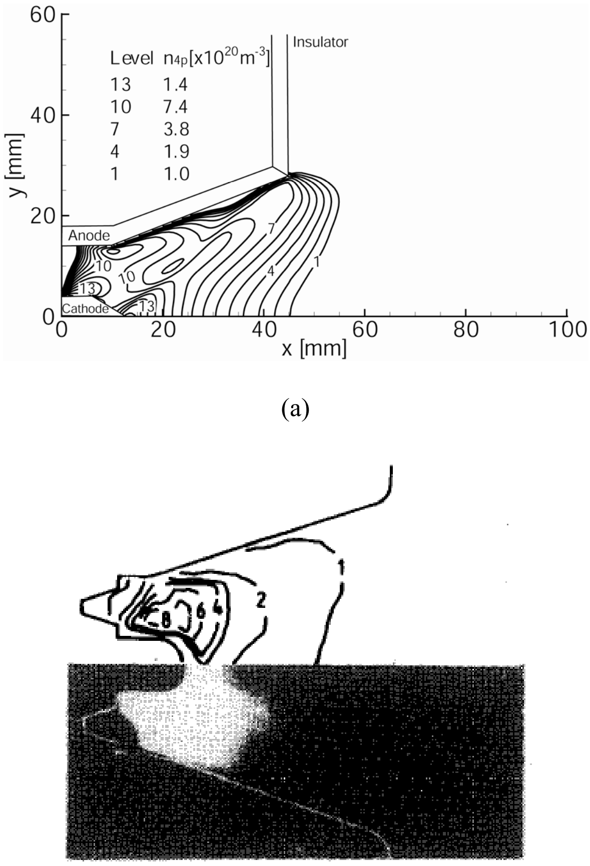

(a)

(b)

Fig. 7. Distribution of excited ion in 4p level, Ar, 1.25 g/s, J = 12 kA, (a) Calc., m^{-3}, (b) Exp., arbitrary unit (From K. Toki, M. Sumida, and K. Kuriki [6], reprinted with permission of the American Institute of Aeronautics and Astronautics, Inc.).

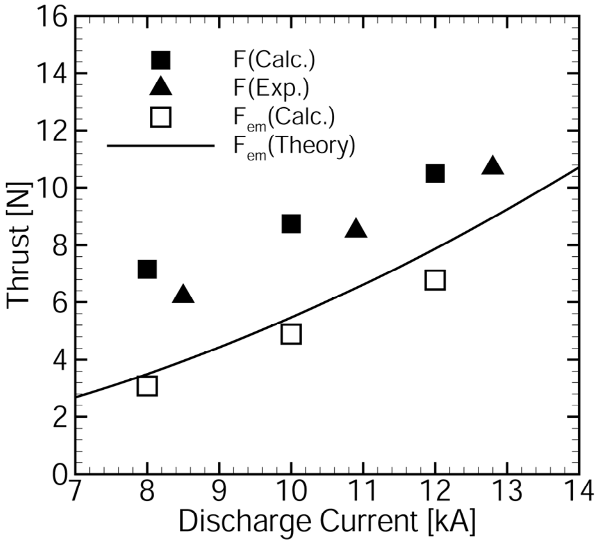

Fig. 8. Thrust vs. discharge current, Ar, 1.25 g/s, Experimental values are referred from [31].

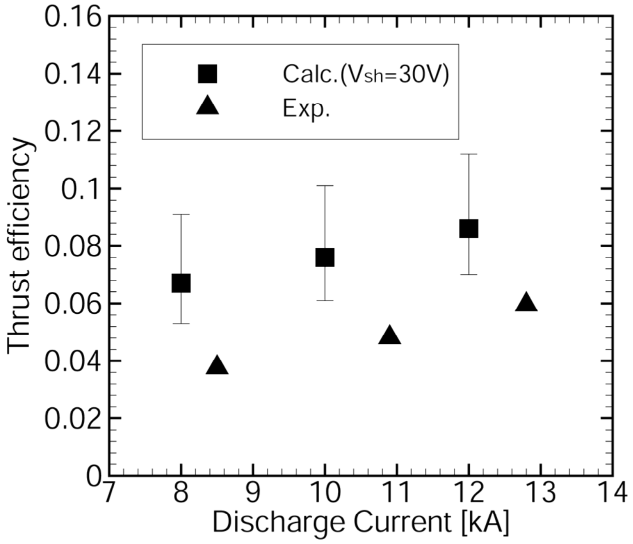

Fig. 9. Thrust efficiency vs. discharge current, Ar, 1.25 g/s, The top and the bottom of the error bar for the calculation results represents the thrust efficiency for the sheath voltage V_{sh} = 20 and 40 V respectively. Experimental values are referred from [31].

Kenichi Kubota received the B.S. degree from the Department of Physics, Tokyo Institute of Technology, Tokyo, Japan, in 2004 and the M.E. and D. E. degrees from the Department of Energy Sciences, Tokyo Institute of Technology, Kanagawa, Japan, in 2006 and 2009, respectively. He is currently a research fellow of Japan Society for the Promotion of Science.

Ikkoh Funaki (M’00) received the B.S. degree from the Department of Aeronautics, Kyoto University, Kyoto, Japan, in 1990 and the M.S. and Ph.D. degrees from the Department of Aeronautics and Astronautics, University of Tokyo, Tokyo, Japan, in 1992 and 1995, respectively. During 1995 and 2001, he was a part-time Lecturer, then a Research Associate with the Institute of Space and Astronautical Science, Kanagawa, Japan, where he engaged himself in developing the microwave discharge ion engines. In 2001, he became a Lecturer with University of Tsukuba, Japan. In 2003, he joined the Department of Space Transportation Engineering, Institute of Space and Astronautical Science, Japan Aerospace Exploration Agency, Kanagawa, Japan, where he is an Associate Professor. His current research interests are in electric and other advanced spacecraft propulsion systems, plasma application in space, and space plasma physics.

Yoshihiro Okuno received the B.E. degree in electrical engineering from the Kyushu Institute of Technology, Fukuoka, Japan, in 1982 and the M.E. and D.E. degrees in energy sciences from Tokyo Institute of Technology, Kanagawa, Japan, in 1984 and 1987, respectively.
He is currently a Professor with the Tokyo Institute of Technology.